https://doi.org/10.1016/j.jpowsour.2023.233779

All-scale investigation of a commercial proton exchange membrane fuel cell with partially narrow channels

Lizhen Wu [a], Guobin Zhang [b, *], Xingyi Shi[a], Zhefei Pan[a], Biao Xie[c], Wenming Huo[c], Kui Jiao [c, d, **] and Liang An[a, ***]

a. Department of Mechanical Engineering, The Hong Kong Polytechnic University, Hung Hom, Kowloon, Hong Kong Special Administrative Region, China

b. MOE Key Laboratory of Thermo-Fluid Science and Engineering, School of Energy and Power Engineering, Xi'an Jiaotong University, Xi'an 710049, China

c. State Key Laboratory of Engines, Tianjin University, 135 Yaguan Road, Tianjin 300350, China

d. National Industry-Education Platform of Energy Storage, Tianjin University, 135 Yaguan Rd, Tianjin 300350, China

* Corresponding author.

** Corresponding author.

*** Corresponding author. Department of Mechanical Engineering, The Hong Kong Polytechnic University, Hung Hom, Kowloon, Hong Kong Special Administrative Region, China.

E-mail addresses: zhangguobin@xjtu.edu.cn (G. Zhang), kjiao@tju.edu.cn (K. Jiao), liang.an@polyu.edu.hk (L. An).

Abstract

Flow field design and optimization are critical for the proton exchange membrane (PEM) fuel cells to meet the requirement of ultra-high power density commercial applications. However, the multi-physics transport mechanism inside such large-scale PEM fuel cells has not been fully understood. In this study, we have developed a three-dimensional (3D) PEM fuel cell model. It is first validated against the experimental data obtained from a small-size cell. Thereafter, based on this model, the performance characteristics of a large fuel cell (cell area: 245.76 cm^2) assembled with a partially narrow flow field are elucidated, while the full bipolar plate (BP) and cell morphology are also considered. It is found that the partially narrow flow field can not only significantly increase the net power density of PEM fuel cells, but also effectively improve the uniform distribution of species with the staggered partially narrow (SPN) zone arrangement between adjacent channels. While this flow field can improve the cell performance, the blindly increasing of the narrow zone numbers may play a negative impact on the net power density due to the dramatic increase in pressure drop. Finally, the partially narrow channel can indeed provide improved drainage capacity.

Keywords: PEM fuel cell; full-morphology simulation; partially narrow channel; power density; drainage.

1. Introduction

In the recent years, the hydrogen economy is widely considered as a promising solution for realizing the goal of carbon neutrality. It utilizes the carbon-free hydrogen as the major energy carrier to replace the conventional fossil fuels and reduce the carbon emission [1]. The accomplishment of hydrogen economy, however, requires the development of various technologies covering from hydrogen production to utilization. Proton exchange membrane (PEM) fuel cell has been widely recognized as a favorable hydrogen-utilization device for its high-efficiency, which possesses great commercial potential for powering future automotive vehicles [2]. By deploying the PEM fuel cell, a number of leading automakers such as Toyota, Honda, Hyundai and SAIC have launched their landmark fuel cell electric vehicles (FCEVs) [3, 4]. Nevertheless, till date, the sluggish oxygen reduction reaction (ORR) [5, 6] on the cathode side of PEM fuel cells has continued being one of the key factors limiting the cell performance [7]. It is therefore a necessary prerequisite for the PEM fuel cells to ensure adequate supply of oxygen before realizing further performance advancement. Considering the critical role of the cathode flow field on affecting the oxygen delivery from the flow channel to the catalyst layer (CL) [8], cathode flow field design and optimization are hence believed to be the important missions for the PEM fuel cell.

It is desired for the flow field to ensure uniform reactant gas distribution, and minimized pressure drop, while creating a good balance between suitable membrane hydration level and efficient drainage to enable the fuel cell with high-power density output [9]. To date, the most common flow field designs can be divided into conventional channel-

rib structures and porous structures [10]. Conventional flow fields with the channel-rib structure such as the parallel and serpentine flow fields [11] are widely used due to their simple pattern and low processing cost. However, at the perpendicular direction of the GDL surface, these conventional designs can only provide a weak advection, thereby confining their mass transfer capability [12]. As a resolution, some state-of-the-art designs construct the flow field by inserting baffles and distributed pins into the flow channel. For example, Wang et al. [13] and Yin et al. [14] demonstrated that the baffle can force more oxygen to flow into the porous electrode while removing liquid water with the help of enhanced convection effect through both simulation and experimental methods. However, Perng et al. [15] found that the baffle design is prone to cause local high temperature and excessive pressure drop in the PEM fuel cells to hinder its performance. Another design with a wave-like channel structure was first adopted by Honda to enhance the convection effect, thereby improving the distribution of reactant gas [16]. Similar designs were also studied by Rahmani et al. [17] through the 3D numerical simulation method, proving that the raccoon flow field can indeed contribute to the uniform gas distribution and efficient drainage at high current densities. Adopting the wave-like flow field design with the change of cross-sectional area, Li et al. [18] boosted the cell peak power density by 13.45% in comparison to the conventional parallel flow field. However, it should be noted that, all the above channel-rib flow field designs are limited by the machining accuracy where the rib width is mostly ~ 0.5-0.8 mm. While with the numerical method, Xie et al. confirmed [19] that the fine channel geometry can effectively improve the uniformity of gas distribution and thereby

enhance the fuel cell performance. Although the current manufacturing technology still cannot achieve all the simulated flow filed designs, the width of channels and ribs can now be effectively reduced to ~0.1 mm granting researchers with wider design flexibility. In addition, it is also mentioned in the literature that when the flow field and rib width are reduced to a certain extent, it can also show effects similar to porous structures [6].

Porous structure flow fields usually construct with a 3D (three-dimensional) interconnected framework, which as a result own a high porosity (greater than 90%) [20]. In recent years, a large number of experimental and simulation studies have shown that such flow fields (e.g., metal foam flow field) can effectively improve the reactant transport, water [21] and thermal management [22], which thereby can grant better cell performance [23]. For instance, Zhang et al. [24] employed a hierarchical porous component (a metal foam coated with a microporous layer (MPL) on its top) to replace the traditional flow field and the gas diffusion layer (GDL), which was found to raise the cell peak power density by 21% at 100% RH. Using the neutron imaging, Wu et al. [25] observed that the metal foam flow field improve the uniformity of liquid water distribution and support the cell to tolerate higher dehydration level. However, the chemical corrosion process needed during the metal form flow field fabrication will cause durability issues thereby resulting in a complex post-processing procedures [26]. Graphene foam flow fields though do not require this kind of after-treatment due to their good corrosion resistance and hydrophobicity [27], possess a weak strength and durability. Using the porous structure flow field design, Toyota made their first

commercial trail by implementing a 3D fine mesh Ti flow field in the fuel cells of the first-generation MIRAI FCEV [28]. However, confined by its high manufacturing cost and the thick end plate that reduces power performance, in the second-generation MIRAI (2021), it was replaced by the flow field with a partially narrow straight channel [29]. This channel design is reported to significantly increase the oxygen concentration in the catalyst layer by a factor of 2.3 compared to a conventional straight channel. Using this flow-field design, the output performance per cell thus can increase by 25%, allowing the number of cells in the latest stack to be greatly reduced from 370 to 330, while the stack power raising from 114 kW to 128 kW. The thickness of the single cell has also reduced from 1.34 to 1.11 mm, where the thickness of the separator has reduced from 0.13 to 0.11 mm. Overall, the cell pack has been reduced a of size 33 to 24 L (excluding end plates), and a weight of from 42 to 24 kg.

Similar to conventional and 3D porous flow fields, the partially narrow flow field is used to ensure the even distribution of reactants in the electrodes. However, in comparison to the conventional flow field, the partially narrow flow field could enhance the convection process of oxygen, which thus could allow a better mass transport process leading to significantly improved cell performance. While different from the 3D porous flow field, it has the advantage of ease of manufacturing, which could reduce the fabrication cost. Attracted by this design, some related studies have also been conducted to explore the influence of the partially narrow flow-field design parameters on its mass transport processes and the cell output performance [30]. However, many studies simply considered the tapered shape along the in-plane direction [31], while

ignoring the possible influences at other directions. Hence, followed with the fuel cell flow field design in the second-generation MIRAI, Zhou et al. [32] innovatively proposed a three-dimensional trapezoidal baffle structure flow field called intercepted flow field (ICFF), where the partially narrowed channels are tapered in all directions and has a staggered structure between adjacent channels. Yet, in their study, the cell was only considered with an activation area of 25 cm^2, which is far from the actual size of ~300 cm^2 in FCEVs.

In this study, the 3D multiphase model of the PEM fuel cell has been developed by further including the liquid cooling channel. The partially narrow channel design has been compared with the conventional channel-rib design (Base) from both top-view and side-view directions. The effects of the partially narrow channel design on the cell output performance, internal transport process and heat transfer process have also been explored. In addition, by adopting the developed model, the effect of array pattern and number of repeated narrow zones have been examined, providing guidance to the channel design optimization in the future.

2. Methods

2.1 Governing equations

The 3D PEM fuel cell model used in this study is an extension of our previous work [7]. In the previous study, we utilized our own developed model to investigate the conventional channel-rib flow fields and porous flow fields. By comprehensively analyzing their effects on the heat and mass transfer process inside a PEM fuel cell, effective flow field design guidelines are given. In addition to the original series of

governing equations describing the gas-water-electricity-heat multiphysics coupling, such as mass, momentum, gas species, liquid pressure, membrane water content, electric potential, ionic potential and energy, the main extension is the addition of governing equations describing coolant flow. The volume of fluid (VOF) method was also used to explore the effect of the partially narrow channel on the drainage capacity. Table 1 summarizes the detailed governing equations mentioned above. Operating conditions and important model parameters are given in Tables 2 and 3. Other details such as model parameters and source terms can be found in the previous study [6].

2.2 Boundary conditions

The velocity is specified at the cooling channel inlets. At the anode and cathode channel inlets, the mass flow rates are described as follows [20]:

$$m_{\mathrm{a}} = \frac{\rho_{\mathrm{g}}^{\mathrm{a}} I \xi_{\mathrm{a}} A_{\mathrm{act}}}{2FC_{\mathrm{H_2}}} \tag{1}$$

$$m_{\mathrm{c}} = \frac{\rho_{\mathrm{g}}^{\mathrm{c}} I \xi_{\mathrm{c}} A_{\mathrm{act}}}{4FC_{\mathrm{O_2}}} \tag{2}$$

$$C_{\mathrm{H_2}} = \frac{P_{\mathrm{g,out}}^{\mathrm{a}} + \Delta P_{\mathrm{g}}^{\mathrm{a}} - RH_{\mathrm{a}} P^{\mathrm{sat}}}{RT} \tag{3}$$

$$C_{\mathrm{O_2}} = \frac{0.21\left(P_{\mathrm{g,out}}^{\mathrm{c}} + \Delta P_{\mathrm{g}}^{\mathrm{c}} - RH_{\mathrm{c}} P^{\mathrm{sat}}\right)}{RT} \tag{4}$$

where m, I, and ξ are the mass flow rate, operating current density, and the stoichiometric ratio, respectively. A_{act} is the area of the MEA (membrane electrode assembly), while C is the species concentration. RH and P^{sat} represent the relative humidity and the water saturation pressure, respectively. At the outlets of gas and cooling channels, constant pressures are specified.

All the waste heat generated in the PEM fuel cell is assumed to be blown away by the coolant flow and the surrounding surfaces of the computational domain are set to be adiabatic, i.e. zero heat flux [10]. The operating current density and reference voltage (0 V) are specified at the anode and cathode endplate surfaces, respectively.

2.3 Numerical implementation

The 3D PEM fuel cell model is implemented in ANSYS FLUENT and the user defined function (UDF) is activated for numerical simulation. Specifically, mass, momentum, species, and energy conservations are solved by Fluent modulus, and the governing equations of electron/proton conduction, membrane water transport and liquid water are solved through the UDF. Figure 1 shows the computational domain. The distribution zones and the other parts are meshed by tetrahedral grids and hexahedral grids respectively. The interface function in ANSYS FLUENT is activated to solve the mismatch issue at the interfaces between the distribution zones and flow fields. There are 11 and 45 million grid points in the PEM fuel cells assembled with parallel and partially narrow channel flow field, respectively. All the simulation cases were conducted on the supercomputer (PARATERA Co. Ltd., Beijing, China). For the simulation case of PEM fuel cell with parallel flow field (or partially narrow flow field), each case took about 72 (or 144) CPU hours with 92 processors running in parallel.

3. Results and discussion

3.1 Model validation

The numerical results have been first compared with the experimental data [33] as shown in Figure 2, where a good agreement is found for the PEM fuel cells with the

partially narrow flow field, demonstrating the reliability of the developed model. The fuel cell geometry and validation parameters are summarized in Table S1 (Supplemental Information). In this small-scale cell (MEA area: 2 cm × 2.2 cm), the increased number of narrow zones is found to significantly improve the cell performance, where the positive impact becomes more and more obvious as the operating current density rises. This is due to the intensified oxygen delivery in the through-plane direction caused by the enhanced convection effect in the narrow zones. However, the performance of PEM fuel cell with PNN1 is close to that of PSN1. The reason for the small difference between the PNN1 and PSN1 is due to the data is originated from a small-scale cell used for testing, which therefore only has a small mass transfer loss leading to an unobvious performance difference. In the following studies, to better simulate the cell performance for actual commercial devices, the numerical simulations are conducted for a large-scale PEM fuel cell with partially narrow flow field.

3.2 Comparison between Base and PPN, SPN

In this section, the performance improvement mechanisms of the PEM fuel cell with the partially narrow channel are explored. As can be seen in Figure 3(a), the partially narrow flow field has demonstrated a better performance, especially at high current density region. It is noteworthy that, while the partially narrow zone will significantly increase the pressure drops in the channel (Figure S1(a)), the net power density of the PEM fuel cell with such flow field has still been greatly improved (excluding pumping loss) as depicted in Figure 3(b). In comparison to the parallel partially narrow (PPN)

zone arrangement between adjacent channels, the staggered partially narrow (SPN) zone arrangement between adjacent channels not only further improves the cell performance, but also enhances the distribution uniformity of current density (Figure 3(c)) and oxygen concentration (Figure 3(d)) at the electrode. Interestingly, with criss-cross pattern coolant channel of the SPN (Figure 1), the cell temperature has also been found to decrease as shown in Figure S1(b) and Figures 4(c-d).

The above-mentioned advantages of SPN mainly come from its special geometry and arrangement, which results in the increase of oxygen concentrations at the electrode (1.78 times higher than that of Base at 3.0 A cm^{-2}). However, as can be seen from Figures 4(c-d), the raise of oxygen concentration would on the other hand lead to the decrease of water vapor permeance, thereby lowering the membrane hydration level to induce a large ionic ohmic loss. Such a competitive relationship between oxygen concentration and water vapor permeability is thus extremely important at low humidity condition, especially when the cell is operated at high operating current density (such as at 3.0A cm^{-2}). Nevertheless, as can be seen from the detailed losses shown in Figures 4(a-b), with the adoption of SPN, the increase in ionic ohmic losses (6.0% and 4.0% compared with base and PPN respectively) is not as pronounced as the decrease in mass transfer losses (28.8% and 11.8% compared with base and PPN respectively) at 3.0A cm^{-2}, which therefore present the SPN as an effective channel design for high-performance PEM fuel cells.

3.3 Effect of distribution zone

From Figure 5(a), it can be seen that with the introduction of the distribution zone, Base,

PPN, and SPN all show a pressure increase trend from channel 1 to channel 80. However, when the distribution zones are removed, the apparent pressure increase trend described above disappears, indicating that the distribution zone enhances lateral oxygen transfer in the GDL. Furthermore, as shown in Figure 5(b), for the SPN with or without distribution zones, the misalignment of narrow zones in adjacent channels results in a significant pressure difference between adjacent channels and further promote the uniform oxygen distribution in the GDL and CL. In contrast, for the PPN, the removement of distribution zones makes the pressure difference between adjacent channels very insignificant, which is due to the parallel arrangement of narrow zones between adjacent channels. The pressure of slices at other positions also shows the similar trend as discussed above (Figure S2), while the SPN can guarantee a much more obvious uniformity advantage in the distribution of various species (Figure S3). Therefore, the necessity of misalignment of narrow zones can be demonstrated by removing the distribution zone.

3.4 Effect of repeated partially narrow zones

In order to maximize the impact of the repeated partially narrow zones on the PEM fuel cell performance, we have first tried to reduce the area of each narrow zone by 4 times while introducing 64 repeating units along the channel. It can be seen in Figure 6(a) that, the increase of repeating units slightly improves the cell performance, while the pressure drop rises significantly as shown in Figure 6(b) leading to a dramatic decrease in net power of PEM fuel cell (Figure S4(a)). It can be concluded that the number of repeating units cannot be increased blindly. The increase of repeating units makes the

distribution of current density and oxygen concentration more uniform (Figure 6(c) and (d)), thus weakening the uniformity difference between PPN and SPN. In addition, due to the oxygen concentration at the CL of SPN is greatly increased (Figure S4(b)), its water vapor concentration is reduced, and its water saturation and membrane water are significantly lower than that of PPN, as shown in Figure S5 (a) and (b). Thus, the increase of repeated units makes PPNs indistinguishable from SPNs. However, it is predictable that the temperature at CL is reduced compared to the partially narrow flow field with less repeated narrow zones due to the enhanced cross-pattern of cooling channels.

3.5 The comparison of drainage between partially narrow and single straight channel

In order to investigate the drainage capacity of the different channel designs without increasing the computational time, we decide to select single channel and used the VOF method to investigate it offline without coupling the electrochemical reaction. The specific boundary condition settings and parameters are given in Supplemental Information (Figure S6). The comparison of the liquid water removal process in the single straight channel and partially narrow channel is shown in Figure 7. The 6 initialization droplets are evenly distributed in the upstream, midstream and downstream of the GDL surface. As for the single straight channel, all droplets are discharged from the channel one after another for about 0.24 s, as shown in Figure 7(a)). Figure 7(b) presents the case where the side walls of the partially narrow channel are hydrophilic and the upper wall is superhydrophilic, and Figure 7(c) is the case where the side walls and the upper wall of the partially narrow channel are superhydrophobic.

From the point of view of the drainage mechanism, they behave very differently. Figure 7(b) shows that when the droplet passes through the narrow zone, it is easily adsorbed to the upper wall of the narrow zone (t = 0.06s). Due to the acceleration effect of the narrow zone (Figure S7), the droplet is blown quickly. On the leeward side, it further becomes a liquid film and merges with the previous liquid films. When all the droplets are completely detached from the GDL surface, the time is only t = 0.07s. This phenomenon can avoid the blockage of liquid water to the porous electrode and facilitate the transport of oxygen. Figure 7(c) shows that the superhydrophobic treatment will cause the droplets to pass quickly (less than 0.003s) when passing through the narrow zone and catch up with the preceding droplets that have not reached the next narrow zone for fusion, and then be discharged together, and finally It is only t = 0.06s when all the droplets are expelled. More details are given in supplemental movies.

4. Summary

Herein, we implemented a three-dimensional multiphase PEM fuel cell model considering full morphology and validated it against experimental data for a small-size cell with partially narrow flow field. Based on this model, the performance characteristics of PEM fuel cells with partially narrow flow field have been investigated comprehensively. It is found that the partially narrow flow field exhibits better net power density after excluding pumping losses, especially at high current densities. Partially narrow flow field can be divided into PPN and SPN according to the arrangement of the narrow zones of adjacent channels. Compared with PPN, the SPN

not only improves the cell performance, but also assists with the uniform distribution of current density and oxygen concentration at the electrode (1.78 times higher than Base at 3.0A cm^{-2}), which is mainly attributed to the misalignment of the narrow zones leading to a significant pressure difference between the adjacent channels. However, the increase in oxygen concentration would also lead to a decrease in water vapor, liquid water saturation and membrane hydration level, which in turn increases the ionic ohmic loss especially at low humidity condition and high current densities (e.g., 3.0A cm^{-2}). Overall, the increase in ionic ohmic loss is not as pronounced as the decrease in mass transfer loss at 3.0 A cm^{-2}. In addition, blindly increasing the narrow zone numbers is found to obviously reduce its net power density due to the dramatic increase in pressure drop, while the increase of repeating units is proved can improve the uniform distribution of current density and oxygen concentration. For the water drainage, it is observed that the motion of the droplet is accelerated as it passes through the narrow zone, while the hydrophilicity of the channel wall would greatly influence the droplet discharge behavior. Specifically, compared to the single straight channel, the hydrophobic partially narrow channel wall treatments can help the droplets to leave GDL surface and be expelled from the channel faster .

Acknowledgements

This work was supported by the National Natural Science Foundation of China (No. 52206112), the Shenzhen Science and Technology Innovation Commission (No. SGDX2020110309520404), the Project funded by China Postdoctoral Science

Foundation (No. 2022M710108) and the Fundamental Research Funds for the Central Universities (No. xzy012021018).

References

[1] Jiao K, Xuan J, Du Q, et al. Designing the next generation of proton-exchange membrane fuel cells. Nature, 2021, 595(7867): 361-369.

[2] Yu X, Chang H, Zhao J, et al. Application of self-adaptive temperature recognition in cold-start of an air-cooled proton exchange membrane fuel cell stack. Energy and AI, 2022, 9: 100155.

[3] Nagulapati V M, Kumar S S, Annadurai V, et al. Machine learning based fault detection and state of health estimation of proton exchange membrane fuel cells. Energy and AI, 2023, 12: 100237.

[4] Full Specs of Toyota MIRAI 2021. Toyota Motor Sales, U.S.A., Inc. (2020). https://www.toyota.com/MIRAI/features/mileage_estimates/3002/3003.

[5] Zhou T, Shan H, Yu H, et al. Nanopore Confinement of Electrocatalysts Optimizing Triple Transport for an Ultrahigh‐Power‐Density Zinc–Air Fuel Cell with Robust Stability. Advanced Materials, 2020, 32(47): 2003251.

[6] Ge J, Peters B. Mass transfer in catalytic depolymerization: External effectiveness factors and serendipitous processivity in stagnant and stirred melts. Chemical Engineering Journal, 2023, 466: 143251.

[7] Wang B, Chen W, Pan F, et al. A dot matrix and sloping baffle cathode flow field of proton exchange membrane fuel cell. Journal of Power Sources, 2019, 434: 226741.

[8] Yin C, Yang H, Liu Y, et al. Numerical and experimental investigations on internal humidifying designs for proton exchange membrane fuel cell stack. Applied Energy, 2023, 348: 121543.

[9] Zhang S, Xu H, Qu Z, et al. Bio-inspired flow channel designs for proton exchange membrane fuel cells: A review. Journal of Power Sources, 2022, 522: 231003.

[10] Zhang G, Wu L, Tongsh C, et al. Structure Design for Ultrahigh Power Density Proton Exchange Membrane Fuel Cell. Small Methods, 2023: 2201537.

[11] Liu M, Fan W, Lu G. Study on mass transfer enhancement of locally improved structures and the application in serpentine and parallel flow fields of PEM fuel cells. International Journal of Hydrogen Energy, 2023.

[12] Suo M, Sun K, Chen R, et al. Oxygen transport in proton exchange membrane fuel cells with metal foam flow fields. Journal of Power Sources, 2022, 521: 230937.

[13] Wang Y, Guan C, Zhang P, et al. Optimal design of a cathode flow field with a new arrangement of baffle plates for a high clean power generation of a polymer electrolyte membrane fuel cell. Journal of Cleaner Production, 2022, 375: 134187.

[14] Yin Y, Wu S, Qin Y, et al. Quantitative analysis of trapezoid baffle block sloping angles on oxygen transport and performance of proton exchange membrane fuel cell. Applied Energy, 2020, 271: 115257.

[15] Perng S W, Wu H W. A three-dimensional numerical investigation of trapezoid baffles effect on non-isothermal reactant transport and cell net power in a PEMFC. Applied Energy, 2015, 143: 81-95.

[16] L. He, M. Hou, Y. Gao, et al., Experimental study of the S-shaped flow fields in

proton exchange membrane fuel cells, Energy Conversion and Management 223 (2020).

[17] Rahmani E, Moradi T, Ghandehariun S, et al. Enhanced mass transfer and water discharge in a proton exchange membrane fuel cell with a raccoon channel flow field. Energy, 2023, 264: 126115.

[18] Li Z, Wang S, Yao S, et al. Experimental and numerical study on improvement performance by wave parallel flow field in a proton exchange membrane fuel cell. Chinese Journal of Chemical Engineering, 2022, 45: 90-102.

[19] Xie B, Zhang G, Xuan J, et al. Three-dimensional multi-phase model of PEM fuel cell coupled with improved agglomerate sub-model of catalyst layer. Energy Conversion and Management, 2019, 199: 112051.

[20] Zhang G, Qu Z, Tao W Q, et al. Porous Flow Field for Next-Generation Proton Exchange Membrane Fuel Cells: Materials, Characterization, Design, and Challenges. Chemical Reviews, 2022.

[21] Wan Z, Sun Y, Yang C, et al. Experimental performance investigation on the arrangement of metal foam as flow distributors in proton exchange membrane fuel cell. Energy Conversion and Management, 2021, 231: 113846.

[22] Azarafza A, Ismail M S, Rezakazemi M, et al. Comparative study of conventional and unconventional designs of cathode flow fields in PEM fuel cell. Renewable and Sustainable Energy Reviews, 2019, 116: 109420.

[23] Wan Z, Yan H, Sun Y, et al. Thermal management improvement of air-cooled proton exchange membrane fuel cell by using metal foam flow field. Applied Energy, 2023, 333: 120642.

[24] Zhang Y, Tao Y, Ren H, et al. A metallic gas diffusion layer and porous media flow field for proton exchange membrane fuel cells. Journal of Power Sources, 2022, 543: 231847.

[25] Yw A , Jisca B , Mwa C , et al. Characterization of water management in metal foam flow-field based polymer electrolyte fuel cells using in-operando neutron radiography - ScienceDirect. International Journal of Hydrogen Energy, 2020, 45(3):2195-2205.

[26] Asri N F, Husaini T, Sulong A B, et al. Coating of stainless steel and titanium bipolar plates for anticorrosion in PEMFC: A review. International Journal of Hydrogen Energy, 2017, 42(14): 9135-9148.

[27] Park J E, Lim J, Kim S, et al. Enhancement of mass transport in fuel cells using three-dimensional graphene foam as flow field. Electrochimica acta, 2018, 265: 488-496.

[28] Yoshida T, Kojima K. Toyota MIRAI fuel cell vehicle and progress toward a future hydrogen society. The Electrochemical Society Interface, 2015, 24(2): 45.

[29] Yoshizumi T, Kubo H, Okumura M. Development of high-performance FC stack for the new MIRAI. SAE Technical Paper, 2021.

[30] Shen J, Du C, Yan F, et al. Enhancement effects of the side blockage arrangement in the flow channel on the performance of a proton exchange membrane fuel cell. International Journal of Energy Research, 2022, 46(12): 16777-16790.

[31] Hu K, Zhao P, Wang S, et al. Three-dimensional Multiphase Simulation of a Partially Narrowed Flow Field Configuration for a High-performance Polymer

Electrolyte Membrane Fuel Cell. Applied Thermal Engineering, 2023: 119986.

[32] Zhou Y, Meng K, Chen W, et al. Experimental performance of proton exchange membrane fuel cell with novel flow fields and numerical investigation of water-gas transport enhancement. Energy Conversion and Management, 2023, 281: 116865.

[33] Ma Y, Gyoten H, Kageyama M, et al. Effects of Partially Narrowed Flow Channel on Performance of Polymer Electrolyte Fuel Cell. ECS Transactions, 2022, 109(9): 171.

Figure and table captions

Figure 1. The computational domain of PEM fuel cell with partially narrow flow field and parallel flow field (base).

Figure 2. Comparison of simulation results and experiment data (PN0: parallel without narrowed structure; PNN3: parallel with neat-arranged 3-mm-long narrowed structures; PNN1: parallel with neat-arranged 1-mm-long narrowed structures; PSN1: parallel with staggered 1-mm-long narrowed structures).

Figure 3. (a) Polarization curves and (b) Net power density of PEM fuel cell with Base, PPN and SPN; (c) Current density distribution in the middle plane of the membrane, and oxygen concentration distribution in the middle plane of the cathode CL at 1.6 A cm^{-2}; and (d) at 3.0 A cm^{-2}.

Figure 4. Comparison of the voltage loss between Base, PPN and SPN: (a) I = 1.6 A cm^{-2}; (b) I = 3.0 A cm^{-2}; Temperature, water vapor concentration, liquid saturation and membrane water distribution in the middle plane of the cathode CL at (c) I =1.6 A cm^{-2}; (d) I = 3.0 A cm^{-2}.

Figure 5. (a) Local static pressure of each channel in slice (Z: 128 mm), (b) Static pressure distribution of channel and GDL (number: 15-18, 41-44) in slice (Z: 128 mm).

Figure 6. Comparison of (a) Output voltage and (b) Pressure drop of PEM fuel cell with PPN, SPN and PPN_64, SPN_64 with increased number of narrow zones; (c) Current density distribution in the middle plane of the membrane, and oxygen concentration distribution in the middle plane of the cathode CL at 1.6 A cm^{-2}; and (d) at 3.0 A cm^{-2}.

Figure 7. Two-phase flow in (a): Base (b): SPN (top wall: 30°, side wall: 60°, GDL surface: 110°); (c): SPN (top wall and side wall: 150°, GDL surface: 110°).

Table 1: Governing equations

Table 2. Geometry parameters and operation conditions

Table 3. Model parameters

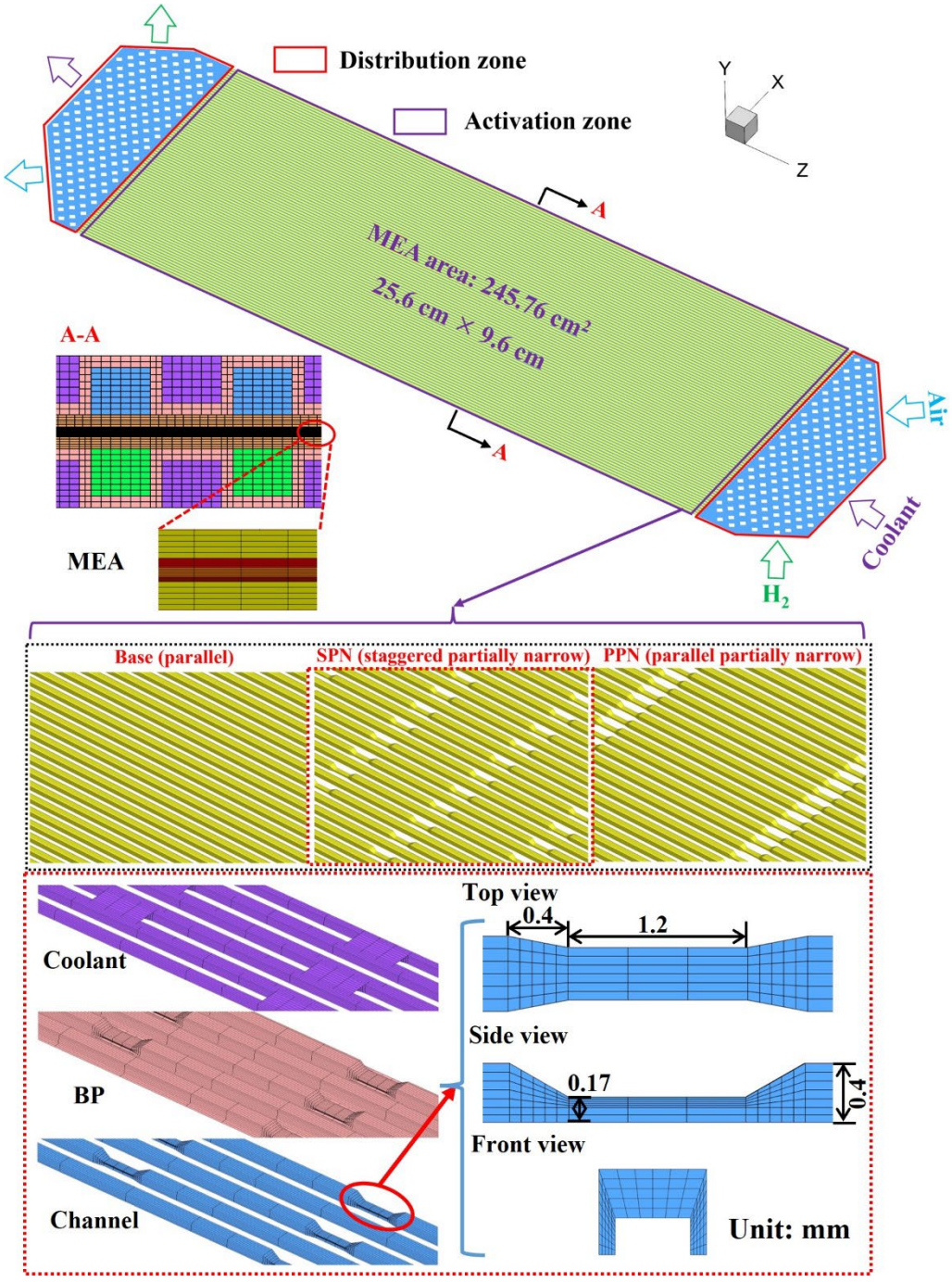

Figure 1. The computational domain of PEM fuel cell with partially narrow flow field and parallel flow field (base).

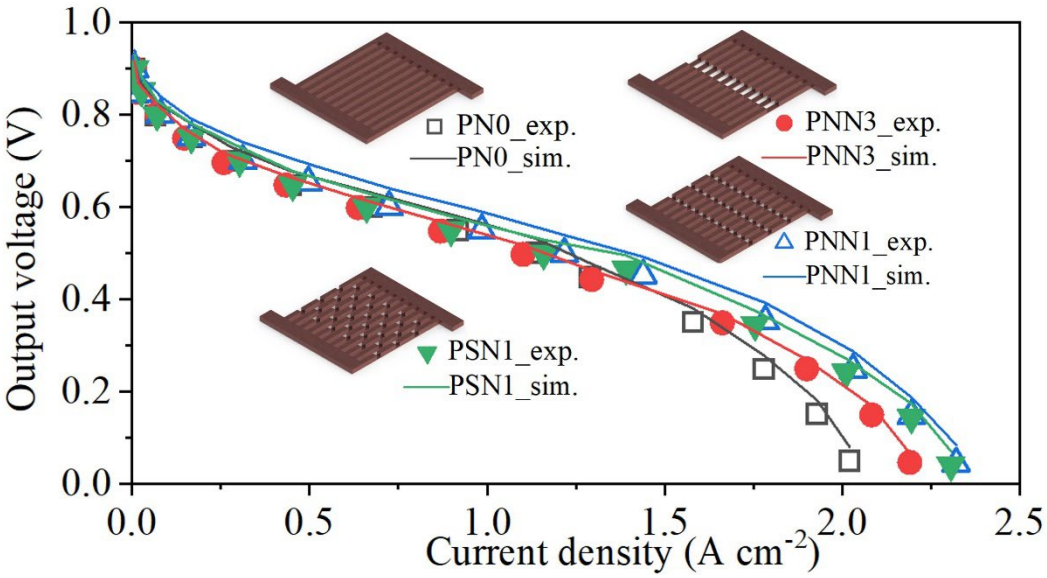

Figure 2. Comparison of simulation results and experiment data (PN0: parallel without narrowed structure; PNN3: parallel with neat-arranged 3-mm-long narrowed structures; PNN1: parallel with neat-arranged 1-mm-long narrowed structures; PSN1: parallel with staggered 1-mm-long narrowed structures).

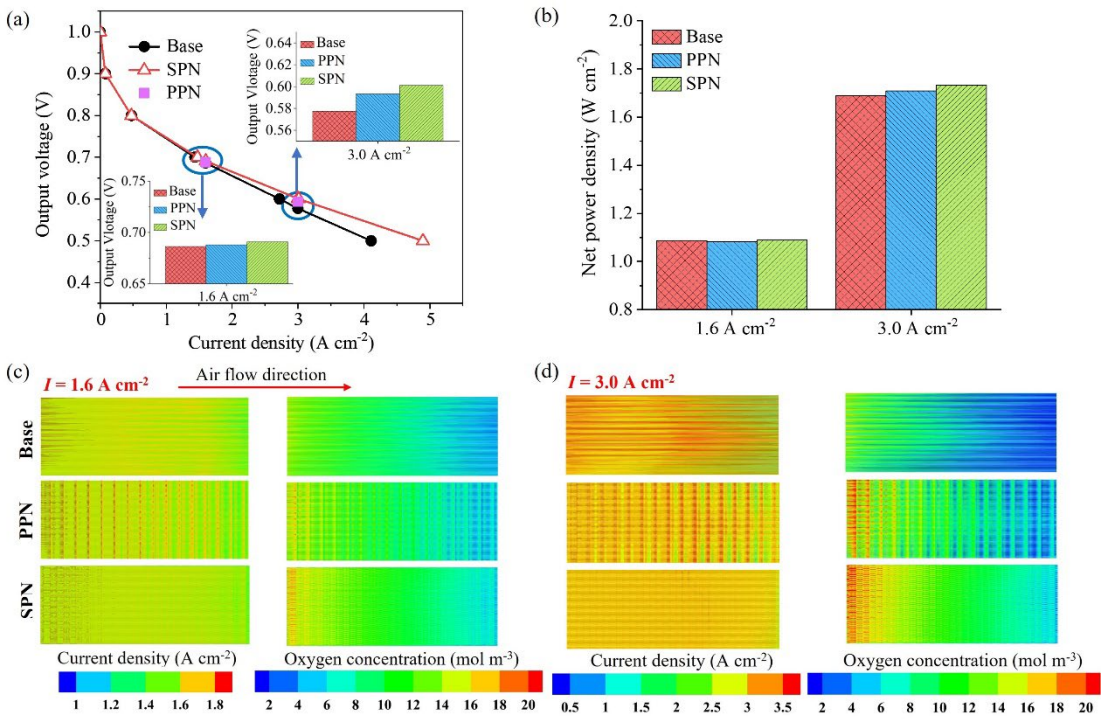

Figure 3. (a) Polarization curves and (b) Net power density of PEM fuel cell with Base, PPN and SPN; (c) Current density distribution in the middle plane of the membrane, and oxygen concentration distribution in the middle plane of the cathode CL at 1.6 A cm^{-2}; and (d) at 3.0 A cm^{-2}.

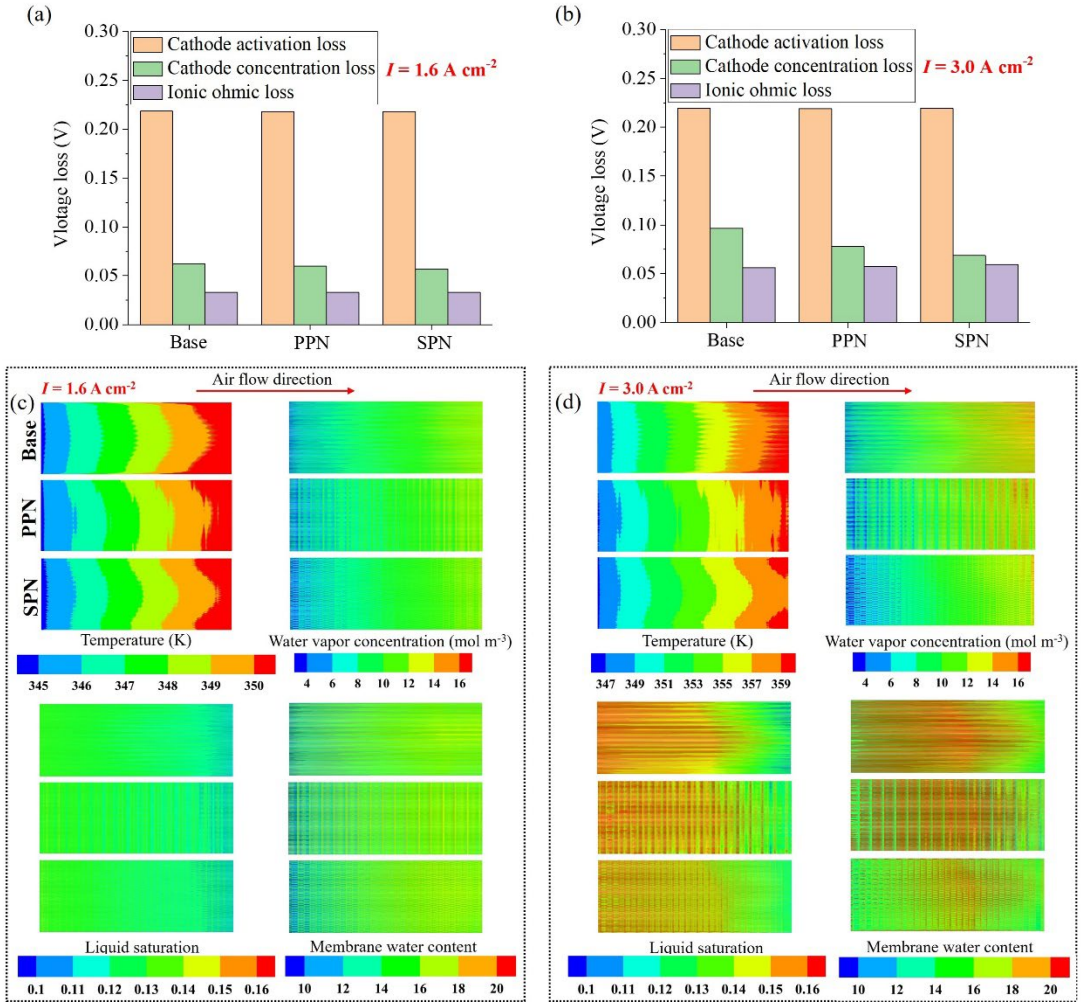

Figure 4 Comparison of the voltage loss between Base, PPN and SPN: (a) I = 1.6 A cm^{-2}; (b) I = 3.0 A cm^{-2}; Temperature, water vapor concentration, liquid saturation and membrane water distribution in the middle plane of the cathode CL at (c) I =1.6 A cm^{-2}; (d) I = 3.0 A cm^{-2}.

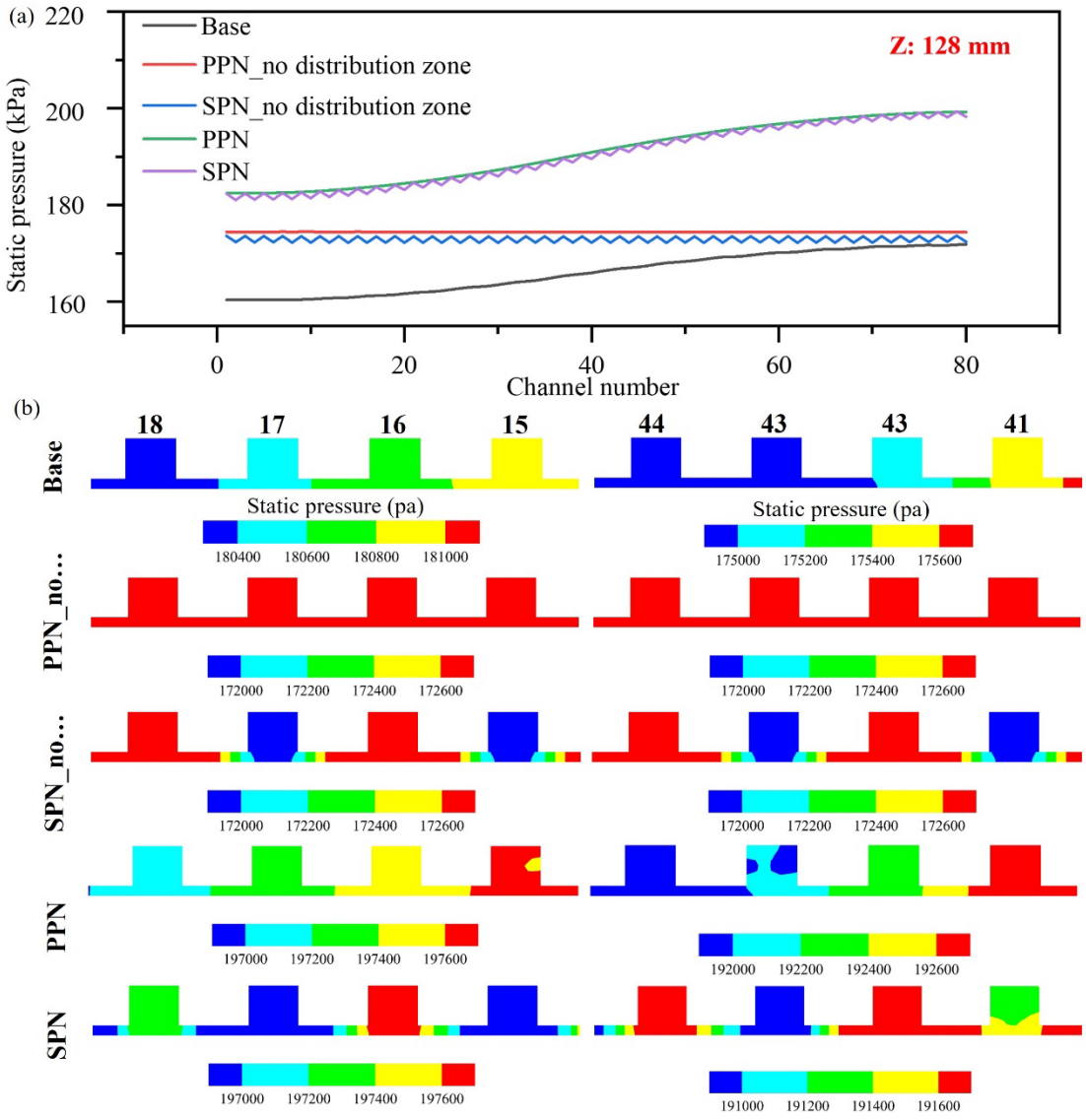

Figure 5. (a) Local static pressure of each channel in slice (Z: 128 mm), (b) Static pressure distribution of channel and GDL (number: 15-18, 41-44) in slice (Z: 128 mm).

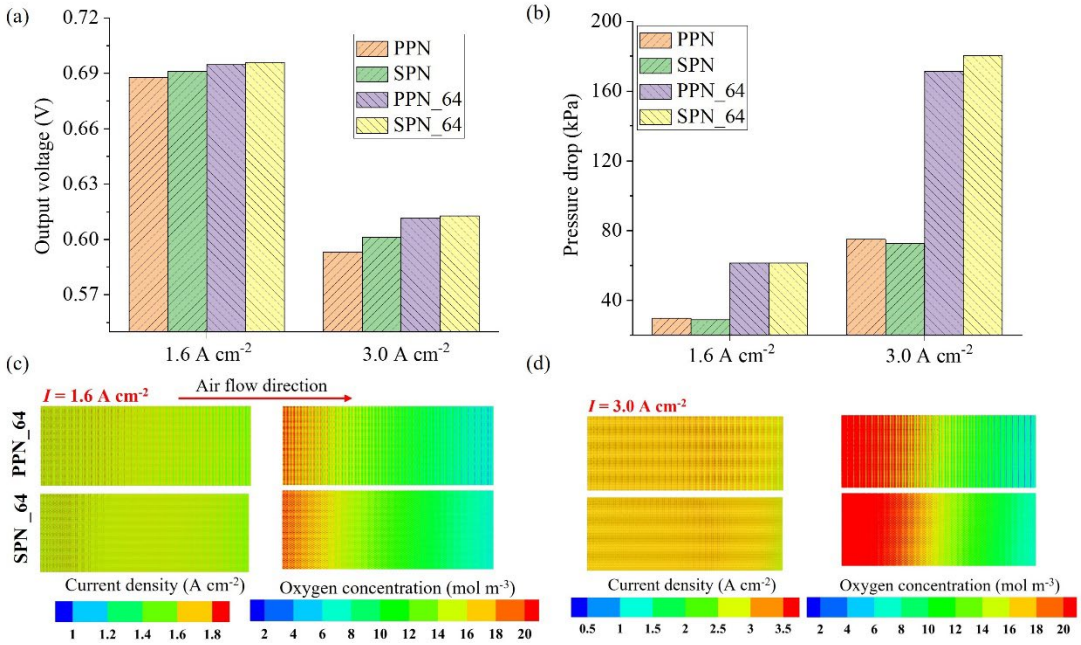

Figure 6. Comparison of (a) Output voltage and (b) Pressure drop of PEM fuel cell with PPN, SPN and PPN_64, SPN_64 with increased number of narrow zones; (c) Current density distribution in the middle plane of the membrane, and oxygen concentration distribution in the middle plane of the cathode CL at 1.6 A cm^{-2}; and (d) at 3.0 A cm^{-2}.

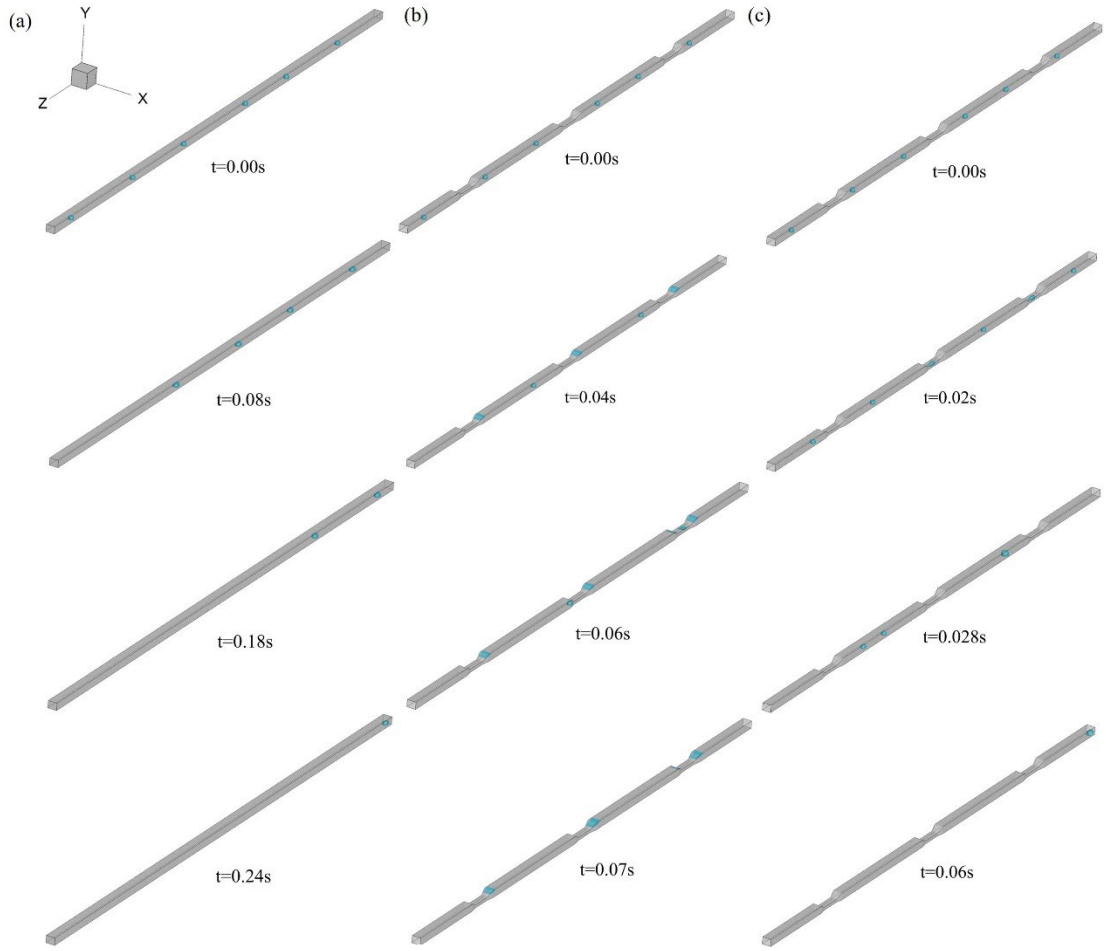

Figure 7. Two-phase flow in (a) Base (b) SPN (top wall: 30°, side wall: 60°, GDL surface: 110°); (c): SPN (top wall and side wall: 150°, GDL surface: 110°).

Table 1. Governing equations

Descriptions	Governing equations
3D full-cell model:	
Mass (coolant)	$\frac{\partial \rho_{\text{cool}}}{\partial t} + \nabla \cdot \left(\rho_{\text{cool}} \boldsymbol{u}_{\text{cool}} \right) = 0$

Momentum (coolant)	$\frac{\partial}{\partial t}\left(\rho_{\text{cool}}\boldsymbol{u}_{\text{cool}}\right)+\nabla\cdot\left(\rho_{\text{cool}}\boldsymbol{u}_{\text{cool}}\boldsymbol{u}_{\text{cool}}\right)=-\nabla P_{\text{cool}}+\mu_{\text{cool}}\nabla\cdot\left(\nabla\boldsymbol{u}_{\text{cool}}\right)$
Mass (coolant)	$\frac{\partial}{\partial t}\left(\varepsilon\left(1-s\right)\rho_{\text{g}}\right)+\nabla\cdot\left(\rho_{\text{g}}\boldsymbol{u}_{\text{g}}\right)=S_{\text{m}}$
Momentum (coolant)	$\frac{\partial}{\partial t}\left(\frac{\rho_{\text{g}}\boldsymbol{u}_{\text{g}}}{\varepsilon\left(1-s\right)}\right)+\nabla\cdot\left(\frac{\rho_{\text{g}}\boldsymbol{u}_{\text{g}}\boldsymbol{u}_{\text{g}}}{\varepsilon^2\left(1-s\right)^2}\right)=-\nabla P_{\text{g}}+\mu_{\text{g}}\nabla\cdot\left(\nabla\left(\frac{\boldsymbol{u}_{\text{g}}}{\varepsilon\left(1-s\right)}\right)+\right.$ $-\frac{2}{3}\mu_{\text{g}}\nabla\left(\nabla\cdot\left(\frac{\boldsymbol{u}_{\text{g}}}{\varepsilon\left(1-s\right)}\right)\right)+\boldsymbol{S}_{\text{ug}}$
Gas species	$\frac{\partial}{\partial t}\left(\varepsilon\left(1-s\right)\rho_{\text{g}}Y_{\text{i}}\right)+\nabla\cdot\left(\rho_{\text{g}}\boldsymbol{u}_{\text{g}}Y_{\text{i}}\right)=\nabla\cdot\left(\rho_{\text{g}}D_{\text{i}}^{\text{eff}}\nabla Y_{\text{i}}\right)+S_{\text{i}}$
Liquid pressure	$\frac{\partial}{\partial t}\left(\rho_{\text{l}}\varepsilon s\right)=\nabla\cdot\left(\rho_{\text{l}}\frac{Kk_{\text{l}}}{\mu_{\text{l}}}\nabla P_{\text{l}}\right)+S_{\text{l}}$
Membrane water content	$\frac{\rho_{\text{mem}}}{\text{EW}}\frac{\partial}{\partial t}\left(\omega\lambda\right)+\nabla\cdot\left(n_{\text{d}}\frac{\boldsymbol{J}_{\text{ion}}}{F}\right)=\frac{\rho_{\text{mem}}}{\text{EW}}\nabla\cdot\left(D_{\text{d}}^{\text{eff}}\nabla\lambda\right)+S_{\text{mw}}$
Electric potential	$0=\nabla\cdot\left(\kappa_{\text{e}}^{\text{eff}}\nabla\varphi_{\text{e}}\right)+S_{\text{e}}$
Ionic potential	$0=\nabla\cdot\left(\kappa_{\text{ion}}^{\text{eff}}\nabla\varphi_{\text{ion}}\right)+S_{\text{ion}}$
Energy	$\frac{\partial}{\partial t}\left(\varepsilon s\rho_{\text{l}}C_{\text{p,l}}T+\varepsilon\left(1-s\right)\rho_{\text{g}}C_{\text{p,g}}T\right)$ $+\nabla\cdot\left(\varepsilon s\rho_{\text{l}}C_{\text{p,l}}\boldsymbol{u}_{\text{l}}T+\varepsilon\left(1-s\right)\rho_{\text{g}}C_{\text{p,g}}\boldsymbol{u}_{\text{g}}T\right)=\nabla\cdot\left(k^{\text{eff}}\nabla T\right)+S_{\text{T}}$
VOF method:	
Mass	$\frac{\partial\rho_{\text{m}}}{\partial t}+\nabla\cdot\left(\rho_{\text{m}}u_{\text{m}}\right)=0$
Momentum	$\frac{\partial\left(\rho_{\text{m}}u_{\text{m}}\right)}{\partial t}+\nabla\cdot\left(\rho_{\text{m}}u_{\text{m}}u_{\text{m}}\right)=-\nabla P+\nabla\cdot\left[\mu_{\text{m}}\left(\nabla u_{\text{m}}+\nabla u_{\text{m}}^{T}\right)\right]+\rho_{\text{m}}g+$
Liquid phase volume fraction	$\frac{\partial s_{\text{l}}}{\partial \text{t}}+v\cdot\nabla s_{\text{l}}=0$

Table 2. Geometry parameters and operation conditions

Parameter	Value
BP thickness (mm)	0.1
Dot diameter (mm)	2.0
The distance between every two dots (mm)	3.74
Channel height (mm)	0.4
Channel/ rib width (mm)	0.5
Channel length (mm)	8
Coolant height (mm)	0.4
Coolant width (mm)	0.5
Gas/coolant channel number	80
GDL thickness (μm)	100.0
MPL thickness (μm)	30.0

Anode CL thickness (μm)	5.0
Cathode CL thickness (μm)	10.0
Membrane thickness (μm)	10.0
Operation pressure (atm)	2.5
Cooling water velocity (m s^{-1})	0.5
Operating temperature (K)	353.15
Gas inlet temperature (K)	353.15
Coolant inlet temperature (K)	343.15
Anode RH	0.3
Cathode RH	0.03
Anode stoichiometric ratio	1.5
Cathode stoichiometric ratio	2.0

Table 3. Model parameters

Parameter	Value
Porosity (GDL, MPL)	0.6, 0.5
Transfer coefficient	Anode: 0.5; Cathode: 0.5
Reference concentration (mol m^{-3})	Hydrogen: 56.4; Oxygen: 3.39
Electric conductivity (GDL, MPL, CL, BP)	3000, 3000, 3000, 20000
Membrane equivalent weight (kg mol^{-1})	1.1
Dry membrane density (kg m^{-3})	1980
Contact angle (GDL, MPL, CL) (°)	110, 120, 95
Permeability (GDL, MPL, CL, membrane) (m^2)	2.0e-12, 1.0e-12, 1.0e-13, 2.0e-20
Condensation/evaporation rate (s^{-1})	100
Membrane water absorption or release rate (s^{-1})	1.3
Henry's constant (Pa m^{-3} mol^{-1})	Hydrogen: 4560; Oxygen: 28000

Pt loading (mg cm^{-2})	Anode: 0.05; Cathode: 0.25
Exchange current density (A m^{-2})	Anode: 8; Cathode:8e-5
Pt/C ratio	Anode: 0.3; Cathode: 0.5
Agglomerate radius (μm)	0.5
Electrolyte film thickness (nm)	150
Electrolyte fraction in agglomerate	0.53
Effective Pt surface ratio	0.5
GDL thermal conductivity (W m^{-1} K^{-1})	21, in-plane; 1.7, through-plane
Thermal conductivity (MPL, CL, membrane, BP) (W m^{-1} K^{-1})	1.0, 1.0, 0.95, 20